Phase-field model of dendritic sidebranching with thermal noise

Alain Karma[1] and Wouter-Jan Rappel[2]
[1]*Department of Physics and Center for Interdisciplinary Research on Complex Systems, Northeastern University, Boston, Massachusetts 02115*
[2]*Department of Physics, University of California, San Diego, La Jolla, California 92093*
(Received 2 February 1999)

We investigate dendritic sidebranching during crystal growth in an undercooled melt by simulation of a phase-field model which incorporates thermal noise of microscopic origin. As a nontrivial quantitative test of this model, we first show that the simulated fluctuation spectrum of a one-dimensional interface in thermal equilibrium agrees with the exact sharp-interface spectrum up to an irrelevant short-wavelength cutoff comparable to the interface thickness. Simulations of dendritic growth are then carried out in two dimensions to compute sidebranching characteristics (root-mean-square amplitude and sidebranch spacing) as a function of distance behind the tip. These quantities are compared quantitatively to the predictions of the existing linear WKB theory of noise amplification. The extension of this study to three dimensions remains needed to determine the origin of noise in experiments. [S1063-651X(99)02010-3]

PACS number(s): 05.70.Ln, 81.30.Fb, 64.70.Dv

I. INTRODUCTION

Dendrites are intricate growth patterns that make up the microstructure of many important commercial alloys [1,2]. They develop a complex shape due to the emission of secondary branches behind the growing tips of primary branches [3]. A major advance in understanding this dynamical process came historically from the insight [4,5] that results of Zel'dovich *et al.* [6] on the stability of flame fronts could be extended to other interfacial pattern forming systems such as dendrites, viscous fingers, etc. For dendrites, further developments along this line [7–11] led to a physical picture where small noisy perturbations, localized initially at the tip, become amplified to a macroscale along the sides of steady-state needle crystals, thereby giving birth to sidebranches [7–11] in qualitative agreement with some experiments [12].

This sidebranching mechanism requires some continuous source of noise at the tip. Therefore, thermal noise, originating from microscopic scale fluctuations inherent in bulk matter, is the most natural and quantifiable candidate to consider. Langer [10] analyzed the amplification of thermal noise along the sides of an axisymmetric paraboloid of revolution and concluded from a rough *estimate* that it is probably not strong enough to explain experimental observations, i.e., sidebranches form closer to the tip in experiment than predicted on the basis of thermal noise amplification. More recently, Brener and Temkin [11] made the interesting observation that noise is amplified faster along the more gently sloping sides of anisotropic (nonaxisymmetric) needle crystals, leading to the conclusion that thermal noise has about the right magnitude to fit experimental data.

There remain, however, several sources of uncertainties regarding this conclusion. First, calculations of noise amplification have been based on a WKB (Wentzel-Kramers-Brillouin) approximation which has only been tested by comparison [8] with numerical simulations [9] for a fixed frequency perturbation localized at the tip. Thermal noise is more difficult to analyze because it involves a wide range of frequencies and is spatially distributed. Consequently, current estimates of the sidebranching amplitude [10,11] involve some overall prefactor which is only known approximately. Secondly, the predicted sidebranching amplitude depends sensitively on the nonaxisymmetric tip shape which seems to vary from system to system. Bisang and Bilgram [13] have found that the tip of xenon dendrites is well fitted by the power law $x \sim z^{3/5}$ [14,15] (as opposed to $x \sim z^{1/2}$ for a paraboloid), where z is the distance behind the tip and x is the radial distance from the growth axis to the interface. In contrast, LaCombe *et al.* [16] find that the tip shape of succinonitrile dendrites is well described up to 10ρ (where ρ is the tip radius) behind the tip by a weak fourfold deviation from a paraboloid $x \sim z^{1/2}$. Since the $z^{3/5}$ power law should only strictly hold far behind the tip [14,15], the proposal [11] that it can be used to predict the sidebranching amplitude remains to be validated beyond the experiments of Bisang and Bilgram [13]. Lastly, analyses of sidebranching have so far been constrained to a linear regime. Therefore, there remains the possibility that nonlinearities produce a noisy limit cycle where sidebranches drive tip oscillations.

At present, it appears to be difficult to make further progress on these issues without some reliable computational approach to accurately simulate dendritic growth with thermal noise. Numerical simulations of dendritic growth using a phase-field approach are consistent with a noise amplification scenario in that sidebranches are absent in purely deterministic simulations where the diffuse interface region is well resolved [17–22]. Moreover, in certain simulations sidebranching has been induced by randomly driving the tip [17,18] in a fashion which is adequate to produce dendritic microstructures, but not to investigate quantitatively the physical origin of sidebranching. In addition, in front-tracking simulations [23], sidebranching appears to be due to the amplification of numerical noise which is difficult to control.

The first goal of this paper is to demonstrate that the phase-field approach [24,25] can be successfully extended to study the effect of thermal noise quantitatively. The second

goal is to use this approach to carry out a quantitative study of sidebranching in order to test the predictions of the linear WKB theory of noise amplification [10,11]. Here, simulations are restricted to two dimensions in order to carry out this comparison in the simplest nontrivial test case. There are two main reasons to elect a phase-field approach to study thermal noise. First, this approach has proven extremely successful to simulate dendritic growth [17–21]. By reformulating the asymptotic analysis of the phase-field model, it has recently been possible to lower the accessible range of undercooling as well as to choose an arbitrary small interface kinetic coefficient [21]. In addition, adaptive mesh refinement methods, used in combination with the reformulated asymptotics, have pushed the limit of undercooling even further towards the experimental range [22]. Secondly, the phase-field approach provides a natural framework to incorporate thermal noise since it is adapted from phenomenological continuum models of second order phase transitions used to study fluctuations near a critical point [26]. Therefore, the formalism to incorporate noise into such models already exists. The extension to the phase-field model mainly requires the use of the fluctuation-dissipation theorem together with an appropriate scaling of parameters to relate the magnitude of the noise in the model with the noise that is present in an experiment. This straightforward exercise is carried out here. An additional issue is the numerical resolution of a small amplitude noise which could be masked by the numerical noise and/or discretization artifacts that are present in simulations. This problem is absent in studies of phase transitions where the bare magnitude of the noise is not important. Here, however, this magnitude plays a crucial role. Fortunately, we shall find that it is possible to resolve accurately a small amplitude noise, of magnitude comparable to experiment, provided that the spatially diffuse interface region is well resolved.

In the context of this study, we are naturally led to revisit the issue of the relative importance of the noises acting in the bulk and at the interface, which was previously considered in the context of a sharp-interface model [27]. Microscopically, the bulk noise originates from fluctuations in the heat current in the solid and liquid phases, whereas the interface noise originates from the exchange of atoms between the two phases (i.e., the attachment and detachment of atoms at the interface). In Ref. [27], it was shown by a direct calculation of the equilibrium fluctuation spectrum of a flat interface that the bulk and interface noises drive, respectively, long-wavelength ($\lambda > \lambda^*$) and short-wavelength ($\lambda < \lambda^*$) regions of this spectrum, where the crossover length $\lambda^* = 4\pi c D/\mu L$. Here, c is the specific heat per unit volume, D the thermal diffusivity, L the latent heat of melting per unit volume, and μ the interface kinetic coefficient. On this basis, it was roughly estimated that the bulk noise should predominantly drive sidebranching whenever $\lambda^* < \lambda_S$, where $\lambda_S \sim \sqrt{D d_0/V}$ is the stability length below which perturbations of the interface are stable, V is the tip velocity, and d_0 is the capillary length. This condition is actually satisfied for growth at low velocity where simple estimations allow one to conclude that $\lambda_S \gg \lambda^*$ for materials with reasonably fast attachment kinetics. In the phase-field model, the bulk and interface noises are represented by Langevin forces added to the evolution equations for the temperature and phase fields, respectively. It is therefore possible to probe the relative importance of these two noises. In this paper, we focus on a low velocity limit where the bulk noise should be dominant according to the above estimate. We observe indeed that sidebranching is unaffected when the noise is switched off in the evolution equation for the phase field, and only the conserved noise is kept in the diffusion equation.

This paper is organized as follows. In Sec. II, we review the sharp-interface equations of solidification with thermal noise and certain useful results of fluctuation theory. In Sec. III, we introduce the phase-field model and analyze its equilibrium fluctuation properties, which allows us to relate the parameters of this model to the known material parameters that enter in the sharp-interface model. In Sec. IV we then discuss the numerical implementation of the model and present the results of a detailed numerical test based on comparing the simulated and analytically predicted fluctuation spectra of a stationary interface in thermal equilibrium. Next, in Sec. V, we present the results of the simulations of dendritic growth and a quantitative comparison of the sidebranching characteristics (amplitude and sidebranch spacing) of a steady-state growing dendrite to the analytical predictions of the WKB theory. Finally, concluding remarks are presented in Sec. VI.

II. SHARP-INTERFACE MODEL

We consider the standard symmetric model with equal thermal diffusivities in the solid and liquid phases. The incorporation of fluctuations in this model, with reference to earlier works, is discussed in detail in Ref. [27] and we only review here the main results. The basic equations of the model are given by

$$\partial_t T = D\,\nabla^2 T - \vec{\nabla}\cdot\vec{j}, \tag{1}$$

$$L V_n = -c\,D\,\hat{n}\cdot(\vec{\nabla}T|_l - \vec{\nabla}T|_s) + c\,\hat{n}\cdot(\vec{j}|_l - \vec{j}|_s), \tag{2}$$

$$T_I = T_M - \Gamma\,\kappa - \frac{V_n}{\mu} + \eta, \tag{3}$$

where $T(\vec{r},t)$ is the temperature field defined in terms of the three-dimensional position vector $\vec{r} = x\hat{x} + y\hat{y} + z\hat{z}$, T_I is the interface temperature, T_M is the melting temperature, $\Gamma = \gamma T_M/L$ is the Gibbs-Thomson coefficient where γ is the surface energy, V_n is the normal velocity of the interface, $\vec{\nabla}T|_l$ ($\vec{\nabla}T|_s$) is the temperature gradient evaluated on the liquid (solid) side of the interface, κ is the interface curvature, and other parameters were defined in Sec. I. The conserved noise, $\vec{j} = j_x\hat{x} + j_y\hat{y} + j_z\hat{z}$, represents the fluctuating part of the heat current, where the components j_m, with $m = x,y,z$, are random variables uncorrelated in space and time that obey a Gaussian distribution. The variance of this distribution,

$$\langle j_m(\vec{r},t) j_n(\vec{r}',t')\rangle = 2\,\frac{D k_B T(\vec{r},t)^2}{c}\,\delta_{mn}\delta(\vec{r}-\vec{r}')\,\delta(t-t'), \tag{4}$$

is fixed by the requirement that the diffusion equation driven by this noise produces, in equilibrium, the known distribution of temperature fluctuations in the solid and liquid phases, which is a simple application of the fluctuation-dissipation theorem. According to basic principles of statistical physics [28], the mean-square fluctuation of the temperature in a small volume ΔV of solid or liquid is given by [28]

$$\langle \Delta T^2 \rangle = \frac{k_B T_M^2}{c \Delta V}, \tag{5}$$

where k_B is the Boltzmann constant, which is precisely the result that one obtains from a simple calculation of $\langle \Delta T^2 \rangle$ using Eq. (1) with $\vec{j}$ defined by Eq. (4). Note that, in a nonequilibrium situation, the temperature variation in the liquid is small compared to the melting temperature, such that $T(\vec{r},t)$ can be replaced by T_M on the right-hand side of Eq. (4).

Next, to write down the correlation of the nonconserved noise that enters in the interface condition (3), it is convenient to define the interface position, $\zeta(\vec{r}_\perp,t) \equiv z_{\rm int}(\vec{r}_\perp,t)$, where $\vec{r}_\perp = x\hat{x} + y\hat{y}$ is the two-dimensional position vector in the plane perpendicular to the z axis. The interface temperature is then simply given by $T_I = T(\vec{r}_{\rm int},t)$, where $\vec{r}_{\rm int} = \vec{r}_\perp + \zeta(\vec{r}_\perp,t)\hat{z}$. We can assume, without loss of generality, that the interface is locally single valued (i.e., no overhang) with respect to this set of coordinates; $\eta(\vec{r}_\perp,t)$ is then Gaussianly distributed with a variance defined by

$$\langle \eta(\vec{r}_\perp,t)\ \eta(\vec{r}'_\perp,t') \rangle = 2 \frac{k_B T_I^2}{\mu L} \frac{\delta(\vec{r}_\perp - \vec{r}'_\perp)\ \delta(t-t')}{\sqrt{1+|\vec{\nabla}_\perp \zeta(\vec{r}_\perp,t)|^2}}, \tag{6}$$

where the square root in the denominator of Eq. (6) is a simple geometrical factor introduced such that the net force on a small area dS of the interface is independent of its local orientation [27], and $\vec{\nabla}_\perp = \hat{x}\partial_x + \hat{y}\partial_y$ denotes the two-dimensional gradient vector in the plane of the interface. The application of the fluctuation-dissipation theorem for this noise requires that its variance be chosen such that the sharp-interface model reproduces the known fluctuation spectrum of a stationary interface in thermal equilibrium, derived analytically in the next section (see also [27]):

$$S(k) \equiv \langle \zeta_k \zeta_{-k} \rangle = \frac{k_B T_M}{\gamma k^2}, \tag{7}$$

where ζ_k is the Fourier coefficient of the interface displacement, i.e.,

$$\zeta(\vec{r}_\perp) = \int \frac{d^2k}{(2\pi)^2} e^{i\vec{k}\cdot\vec{r}_\perp}\ \zeta_k . \tag{8}$$

A straightforward but lengthy calculation described in Ref. [27] shows that Eqs. (1)–(3), with the noises defined by Eqs. (4) and (6), yields this spectrum in equilibrium.

III. PHASE-FIELD MODEL

The Langevin formalism to incorporate fluctuations into continuum models of phase transitions is well established [26], and the same procedure can be followed for the phase-field model. As in the sharp-interface model [27], we proceed by adding stochastic forces whose magnitudes are determined by making contact with equilibrium properties. For this purpose, it is convenient to express the phase-field model in terms of the dimensionless temperature field

$$u = \frac{T - T_M}{L/c}, \tag{9}$$

and the local enthalpy per unit volume defined by

$$H = e_0 \left(u - \frac{p(\phi)}{2} \right), \tag{10}$$

where e_0 is a constant with units of energy per unit volume, ϕ is the phase field chosen to vary between -1 in the liquid and $+1$ in the solid, and $p(\phi)$ is some monotonously increasing function of ϕ with the limiting values $p(\pm 1) = \pm 1$. The phase-field model expressed in terms of these variables takes the form

$$\frac{\partial \phi}{\partial t} = -\Gamma_\phi \frac{\delta \mathcal{F}}{\delta \phi} + \theta(\vec{r},t), \tag{11}$$

$$\frac{\partial H}{\partial t} = \Gamma_H \nabla^2 \frac{\delta \mathcal{F}}{\delta H} - \vec{\nabla} \cdot \vec{q}(\vec{r},t), \tag{12}$$

which is a form similar to Model C of Halperin, Hohenberg, and Ma [26], i.e., with coupled nonconserved (ϕ) and conserved (H) order parameters, which is most naturally suited to add fluctuations. The fact that H is conserved, which follows from Eq. (12), simply reflects the fact that the total energy in a given volume is conserved in the absence of energy fluxes through the surfaces bounding this volume. Next, the free energy is defined by

$$\mathcal{F} = \int d^3r \left[\frac{K}{2} |\vec{\nabla}\phi|^2 + h_0 f(\phi) + e_0 \frac{u^2}{2} \right], \tag{13}$$

where h_0 and K are constants with units of energy per unit volume and per unit length, respectively, and $f(\phi)$ is a double well potential with minima at $\phi = \pm 1$. Specific choices for $p(\phi)$ and $f(\phi)$ will be given in the next section to carry out the computations. Finally, the noises are Gaussianly distributed with variances

$$\langle \theta(\vec{r},t)\, \theta(\vec{r}',t) \rangle = 2\Gamma_\phi k_B T_M \delta(\vec{r} - \vec{r}')\, \delta(t-t'), \tag{14}$$

$$\langle q_m(\vec{r},t) q_n(\vec{r}',t) \rangle = 2\Gamma_H k_B T_M\ \delta_{mn} \delta(\vec{r} - \vec{r}')\, \delta(t-t'). \tag{15}$$

Let us now briefly analyze the equilibrium bulk and interface fluctuations in this diffuse interface model in order to make contact with the sharp-interface model of the preceding section. As is well known, the probability $P[\phi,u;t]$ of finding the system in a given configuration, $\phi(\vec{r},t)$ and $u = u(\vec{r},t)$, at time t is governed by a generalized Fokker-

Planck equation [26] associated with the Langevin equations (11) and (12). For a general nonequilibrium situation, this Fokker-Planck equation has no known analytical solution. In equilibrium, however, it has a time-independent stationary solution

$$P_{\mathrm{eq}}[\phi,u]=\frac{1}{Z}\exp\left(-\frac{\mathcal{F}}{k_B T_M}\right), \tag{16}$$

which allows us to calculate analytically the equilibrium Gaussian fluctuations. Here,

$$Z\equiv\int \mathcal{D}\phi\mathcal{D}u\,\exp\left(-\frac{\mathcal{F}}{k_B T_M}\right) \tag{17}$$

is the equilibrium partition function where $\mathcal{D}\phi$ and $\mathcal{D}u$ denote functional integration over the fields ϕ and u, respectively. Let us first calculate the temperature fluctuations in the bulk phases. Since ϕ is constant in the solid or liquid, only the term $\sim u^2$ in the integrand of $\mathcal{F}$ needs to be kept. Consequently, Eq. (16) implies that the fluctuation of u inside a small volume ΔV is given by

$$\langle u^2\rangle=\int_{-\infty}^{+\infty}du\,u^2\exp\left[-\frac{\Delta V e_0}{k_B T_M}\frac{u^2}{2}\right]\Bigg/\int_{-\infty}^{+\infty}du \times\exp\left[-\frac{\Delta V e_0}{k_B T_M}\frac{u^2}{2}\right], \tag{18}$$

which yields at once the result

$$\langle u^2\rangle=\frac{k_B T_M}{e_0\Delta V}. \tag{19}$$

Now comparing Eq. (19) with Eq. (5) allows us to determine

$$e_0=\frac{L^2}{T_M c}. \tag{20}$$

This result can be obtained, alternatively, by comparing the phase-field equations (12) and (15), in a region where ϕ is constant, with the sharp-interface equations (1) and (4), which yields, in addition, the expression for the diffusion constant

$$D=\frac{\Gamma_H}{e_0}. \tag{21}$$

Next, the equilibrium fluctuations of a stationary interface can be calculated provided that we restrict our attention to wavelengths that are large compared to the width of the spatially diffuse interface region. Let us consider the fluctuations about a flat interface in the plane $z=0$. For a small amplitude deformation, $\zeta(\vec{r}_\perp)$, which varies slowly on the scale of the interface thickness, the phase field can be approximated in the form

$$\phi(\vec{r})\approx\phi_0(z-\zeta(\vec{r}_\perp)), \tag{22}$$

where $\phi_0(z)$ is the solution of the one-dimensional stationary interface problem

$$K\frac{d^2\phi_0(z)}{dz^2}+h_0 f_\phi(\phi_0(z))=0, \tag{23}$$

where we have defined $f_\phi\equiv df/d\phi$. We can then evaluate the gradient term in Eq. (13) using Eq. (22), which yields

$$\vec{\nabla}\phi(\vec{r})\approx\frac{d\phi_0}{dz}[\hat{z}-\vec{\nabla}_\perp\zeta(\vec{r}_\perp)]. \tag{24}$$

Next, we substitute Eqs. (22) and (24) into Eq. (13), which allows us to express the probability distribution (16) directly in terms of $\zeta(\vec{r}_\perp)$ instead of $\phi(\vec{r})$. One immediate simplification is that the one-dimensional part $\int dz$ of the volume integral $\int d^3r=\int d^2r\int dz$ in Eq. (13), where $d^2r\equiv dxdy$, can be carried out explicitly. The resulting integrals proportional to $\int dz f(\phi_0(z-\zeta(\vec{r}_\perp)))$ and $\int dz(d\phi_0/dz)^2$, where the second integral originates from the term $(d\phi_0/dz)\hat{z}$ on the right-hand side of Eq. (24) give only constant contributions independent of $\zeta(\vec{r}_\perp)$. They do not affect the fluctuation probability since they can be factored out of both the numerator $\exp(-\mathcal{F}/k_B T_M)$ and the denominator Z of Eq. (16). Only the gradient term on the right-hand side of Eq. (24) gives a nontrivial ζ-dependent contribution and leads to the expression for the probability distribution of interface fluctuations

$$P[\zeta(\vec{r}_\perp)]=\frac{1}{Z}\exp\left(-\frac{\gamma}{k_B T_M}\int d^2r\frac{1}{2}|\vec{\nabla}_\perp\zeta(\vec{r}_\perp)|^2\right), \tag{25}$$

where

$$Z=\int\mathcal{D}\zeta\exp\left(-\frac{\gamma}{k_B T_M}\int d^2r\frac{1}{2}|\vec{\nabla}_\perp\zeta(\vec{r}_\perp)|^2\right), \tag{26}$$

and

$$\gamma=\sqrt{Kh_0}\int_{-\infty}^{+\infty}d\bar{z}\left[\frac{d\phi_0}{d\bar{z}}\right]^2\equiv\sqrt{Kh_0}\,I \tag{27}$$

is the surface energy; the integral I defined in terms of the dimensionless variable $\bar{z}=z\sqrt{h_0/K}$ is a numerical constant that depends on the form of $f(\phi)$. The result of Eq. (7) stated earlier is now simply obtained by changing variables from $\zeta(\vec{r}_\perp)$ to ζ_k in the probability distribution above, and by using this distribution to calculate $\langle\zeta_k\zeta_{-k}\rangle$, which only involves a Gaussian integral. This simple exercise shows that the interface fluctuations in the phase-field model are identical to those of the sharp-interface model on scales larger than the interface thickness, i.e., $k^{-1}\gg\sqrt{K/h_0}$, as one would naively expect. Finally, Eqs. (20) and (27) can be used to relate the parameters of the phase-field model to the capillary length, $d_0=\gamma T_M c/L^2$, which yields

$$d_0=I\sqrt{\frac{Kh_0}{e_0^2}}. \tag{28}$$

IV. NUMERICAL IMPLEMENTATION

A. Choice of functions and scalings

To carry out numerical simulations, it is convenient to choose the functions

$$f(\phi) = -\phi^2/2 + \phi^4/4, \tag{29}$$

$$p(\phi) = 15(\phi - 2\phi^3/3 + \phi^5/5)/8, \tag{30}$$

where Eq. (29) is the standard quartic form of the double well potential and the form (30) has the advantage that it preserves the minima of ϕ at ± 1 independently of the local value of u [29]. The one-dimensional stationary profile solution of Eq. (23) is then given by

$$\phi_0(z) = -\tanh\left(\frac{z}{\sqrt{2}W}\right), \tag{31}$$

where

$$W = \sqrt{\frac{K}{h_0}} \tag{32}$$

is the interface thickness. Evaluating the integral in Eq. (27) with the above form of $\phi_0(z)$ yields $I = 2\sqrt{2}/3$.

It is useful to express the phase-field equations in a dimensionless form that minimizes the number of computational parameters and that renders the interpretation of the noise magnitude in the phase-field model more transparent. For this purpose, it is useful to define, in addition to W, the time

$$\tau = \frac{1}{\Gamma_\phi h_0}, \tag{33}$$

which characterizes the relaxation of ϕ to one of its local minima, and the coupling constant [30]

$$\Lambda = \frac{e_0}{J h_0} = \frac{I}{J}\frac{1}{\overline{d_0}}, \tag{34}$$

expressed in terms of the scaled capillary length

$$\overline{d_0} = \frac{d_0}{W}. \tag{35}$$

Here, $J = 16/15$ is a constant whose value is fixed by the choice of $p(\phi)$ [21]. We then measure all lengths in units of W and time in units of τ, and define accordingly new dimensionless coordinates, diffusivity, and noise variables, via the substitutions

$$\vec{r}/W \to \vec{r}, \tag{36}$$

$$t/\tau \to t, \tag{37}$$

$$D\tau/W^2 \to D, \tag{38}$$

$$\tau\theta \to \theta, \tag{39}$$

$$\frac{\tau}{e_0 W}\vec{q} \to \vec{q}. \tag{40}$$

Transforming the phase-field equations (11) and (12) with the help of these substitutions, and using the fact that $\delta(\vec{r} - \vec{r}')$ and $\delta(t - t')$ on the right-hand side of Eqs. (14) and (15) have dimensions of $(\text{length})^{-d}$, where d is the dimension, and inverse time, respectively, we obtain the dimensionless form

$$\frac{\partial \phi}{\partial t} = \nabla^2\phi + \phi - \phi^3 - \Lambda\, u\,(1-\phi^2)^2 + \theta(\vec{r},t), \tag{41}$$

$$\frac{\partial u}{\partial t} = D\,\nabla^2 u + \frac{1}{2}\frac{\partial p(\phi)}{\partial t} - \vec{\nabla}\cdot\vec{q}(\vec{r},t), \tag{42}$$

with

$$\langle \theta(\vec{r},t)\,\theta(\vec{r}',t)\rangle = 2F_\phi\,\delta(\vec{r}-\vec{r}')\,\delta(t-t'), \tag{43}$$

$$\langle q_m(\vec{r},t) q_n(\vec{r}',t)\rangle = 2\,D\,F_u\,\delta_{mn}\delta(\vec{r}-\vec{r}')\,\delta(t-t'), \tag{44}$$

and the definitions

$$F_{\text{expt}} = \frac{k_B T_M^2 c}{L^2 d_0^d}, \tag{45}$$

$$F_u = \frac{k_B T_M^2 c}{L^2 W^d} = \overline{d_0^d}\,F_{\text{expt}}, \tag{46}$$

$$F_\phi = \Lambda J F_u. \tag{47}$$

The above definitions allow us to relate the magnitude of the noise which enters into the phase-field model, F_u, with the magnitude of the noise in experiments, F_{expt}. Comparing the right-hand side of Eq. (45), for $d = 3$, with the right-hand side of Eq. (19), we can readily see that F_{expt} is simply equal to the mean-square fluctuation of u inside a microscopic volume d_0^3, and is a fixed quantity for a given material. (Note that F_{expt} can also be written in the form $k_B T_M/\gamma d_0^2$, which is the square of the ratio of two microscopic lengths, $\sqrt{k_B T_M/\gamma}$ and d_0.) The first equality in Eq. (46) implies that F_u is the mean-square fluctuation of u inside a microscopic volume W^3. The second equality dictates how to choose F_u in a simulation for a given system (F_{expt}) and a given choice of computational parameter, $\overline{d_0}$. The dependence on the latter quantity has a simple physical interpretation. Namely, if one chooses $\overline{d_0}$ to be small compared to unity, which is the main gain in computational efficiency resulting from the reformulated asymptotics of Ref. [21], then one must scale down the magnitude of the noise in the phase-field model to keep the fluctuation strength in a physical volume d_0^3 constant. The main practical conclusion here is that one still has the computational freedom to choose the interface thickness if one rescales appropriately the noise strength.

B. Discretization

The phase-field equations (41) and (42) are discretized on an $N\times N$ square lattice of spacing $\Delta x=\Delta z$ using centered finite difference formulas, as described in Ref. [21], and the equations are time stepped using a first order Euler scheme with a time step Δt. The only new elements here are the noises. To see how to discretize them, let $i\Delta x$ and $j\Delta z$ denote the position on the lattice along x and z, respectively. For the nonconserved noise, we generate one random number per lattice site, θ_{ij}, chosen from a Gaussian distribution with a variance

$$\langle \theta_{ij}\theta_{i'j'}\rangle=\frac{2F_\phi}{\Delta t\,\Delta x^2}\delta_{ii'}\delta_{jj'}, \tag{48}$$

where the factors $1/\Delta t$ and $1/\Delta x^2$ on the right-hand side of Eq. (48) are related to the inverse time and the inverse area (inverse volume in three dimensions) scalings of $\delta(t-t')$ and $\delta(\vec{r}-\vec{r}')$, respectively, in the correlation of the noises. θ_{ij} is then added to the deterministic part of the right-hand side of Eq. (41) discretized at site (i,j).

To discretize the conserved noise, we define by $q_{x,ij}$ the current on the bond that links site (i,j) with site $(i+1,j)$, and by $q_{z,ij}$ the current on the bond that links site (i,j) and $(i,j+1)$. We then generate at each time step two independent random numbers per site, $q_{x,ij}$ and $q_{z,ij}$, chosen from a Gaussian distribution with a variance

$$\langle q_{m,ij}q_{n,i'j'}\rangle=\frac{2DF_u}{\Delta t\,\Delta x^2}\delta_{mn}\delta_{ii'}\delta_{jj'}. \tag{49}$$

The divergence of the current on the right-hand side of Eq. (42) at site (i,j) is then discretized in the form

$$(\vec{\nabla}\cdot\vec{q})_{ij}=[q_{x,ij}-q_{x,i-1j}+q_{z,ij}-q_{z,ij-1}]/\Delta x. \tag{50}$$

C. Planar interface fluctuation spectrum

As a nontrivial test of the numerical implementation of the phase-field model, we first calculate the fluctuation spectrum of a one-dimensional stationary interface in thermal equilibrium and compare this spectrum to the analytical prediction (7). With length measured in units of W, Eq. (7) becomes

$$S(k)=\frac{F_u}{\overline{d}_0k^2}, \tag{51}$$

where $\overline{d}_0=I/(J\Lambda)=5\sqrt{2}/8\Lambda$ for the present choice of phase-field model.

To calculate $S(k)$, phase-field simulations were carried out with periodic boundary conditions in x on a lattice of size 512×50 with $\Delta x=0.8$. We used initial conditions that correspond to a flat interface inside a system uniformly at the melting temperature, which corresponds to choosing $\phi=\phi_0(z)=-\tanh(z/\sqrt{2})$ and $u=0$. The interface profile, $\zeta(x)$, is defined by $\phi(x,\zeta(x))=0$, and is calculated by finding the $\phi=0$ contour of the phase field by interpolation at each time step. The complex amplitude, ζ_k, is then calculated by a one-dimensional fast Fourier transform where ζ_k and $\zeta(x)$ are related by

$$\zeta(x)=\int\frac{dk}{2\pi}e^{ikx}\zeta_k, \tag{52}$$

Finally, $S(k)=\langle|\zeta_k|^2\rangle$ is calculated by taking a time average of $|\zeta_k|^2$. Long simulations with typically 10^5 to 10^6 time steps were necessary to obtain good statistics. These calculations were carried out by using Eq. (42) with both $p(\phi)$ defined by Eq. (30) and $p(\phi)=\phi$. Note that the constant $J=16/15$ is the same for both choices [21] since the form of the phase-field equation (41) is unchanged, and thus derived from $p(\phi)$ defined by Eq. (30) in both cases. Of course, with Eq. (41) unchanged and the choice $p(\phi)=\phi$ in Eq. (42), the phase-field equations are no longer variational (i.e., derivable from a Lyapounov functional), but the sharp-interface limit remains identical and the interface can be resolved with a larger Δx, as shown previously [21]. The spectra for the two choices of $p(\phi)$ were found to be virtually indistinguishable such that only the results for $p(\phi)=\phi$ are reported here. In the dendritic growth simulations presented below, we will restrict our attention solely to the case where $p(\phi)=\phi$ is used as the source of latent heat in the heat equation.

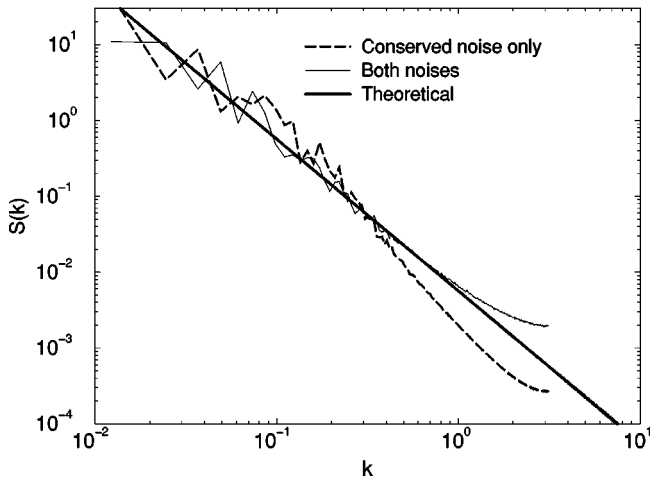

FIG. 1. Simulated spectra of a one-dimensional interface in thermal equilibrium with both nonconserved and conserved noises (thin solid line) and only the conserved noise (dashed line), compared to the theoretical prediction of Eq. (51) (thick solid line). Length is measured in units of W. Parameters used in simulations are $\Lambda=1$, $D=1$, and $F_u=0.005$.

Spectra obtained for a typical set of computational parameters are compared in Fig. 1 with the analytical prediction (51), represented by a thick solid line, both for the case where the nonconserved and conserved noises are added to the phase-field equations (thin solid line with $F_u\neq 0$ and $F_\phi\neq 0$) and for the case where the nonconserved noise is switched off in the ϕ equation (dashed line with $F_u\neq 0$ but $F_\phi=0$). With both noises present, the calculated spectrum agrees well with the theoretical prediction up to a cutoff in k of order unity (corresponding to a wavelength comparable to the interface thickness in physical units). With only the conserved noise present ($F_\phi=0$), the simulated spectrum follows initially well the predicted $1/k^2$ law with increasing k,

but then drops off rapidly to a very small amplitude at large k. This dropoff is consistent with the analytical prediction of Ref. [27] and is due to the extra dissipation at the interface that damps out short scale fluctuations.

D. Incorporation of anisotropy

In order to investigate dendritic sidebranching in the next section, we incorporate anisotropy as other authors have [31,32] by letting the coefficient of the gradient energy term in the free energy depend on the normal to the solid-liquid interface, $\hat{n}=\vec{\nabla}\phi/|\vec{\nabla}\phi|$. Following this change, Eq. (42) remains unchanged and Eq. (41) becomes

$$f_k(\hat{n})\,\partial_t\phi=\phi-\phi^3-\Lambda\,u\,(1-\phi^2)^2+\vec{\nabla}\cdot[f_s(\hat{n})^2\vec{\nabla}\phi]+\sum_{m=x,z}\partial_m\left(|\vec{\nabla}\phi|^2 f_s(\hat{n})\frac{\partial f_s(\hat{n})}{\partial(\partial_m\phi)}\right)+\theta(\vec{r},t), \tag{53}$$

where we have defined the anisotropy function for a crystal with an underlying cubic symmetry

$$f_s(\hat{n})=1-3\epsilon_4+4\epsilon_4(\partial_x^4\phi+\partial_z^4\phi)/|\vec{\nabla}\phi|^4. \tag{54}$$

We neglect the orientation dependence of the noise strength, which is in principle simple to include, and therefore define the variance of $\theta(\vec{r},t)$ by Eq. (43). This turns out to be unimportant here since this noise does not affect sidebranching in the simulations presented in the next section. As in our previous study of dendritic growth without noise [21], we use the result of a reformulated asymptotic analysis of the phase-field model together with a method to compute lattice corrections to the surface energy and kinetic anisotropies. Moreover, we focus on a choice of computational parameters that makes $1/\mu$ vanish in the interface condition (3). The effective anisotropy of the phase-field model, which includes lattice corrections, is given at order Δx^2 by

$$\epsilon_e=\epsilon_4-\Delta x^2/240. \tag{55}$$

Here, we use $\Delta x=0.8$, and input the value $\epsilon_4=0.032\,66$ into Eq. (54) to obtain an effective anisotropy $\epsilon_e=0.03$ when comparing our results to the sharp-interface solvability theory. This 3% anisotropy leads to a relatively large stiffness anisotropy $15\epsilon_e=0.45$. This choice was made to allow us to carry out long simulation runs that are necessary to calculate accurately noise-averaged quantities such as the sidebranching amplitude and spacing on a uniform grid. Decreasing the anisotropy at fixed undercooling reduces the interface velocity (increases the diffusion length) and thus increases substantially the computational domain size and simulation time. In addition, this stiffness is comparable to that of Pivalic acid (PVA) used in dendritic growth experiments [33]. (The most recent anisotropy measurement [34] yields a 2.5% surface energy anisotropy equivalent to a stiffness anisotropy of 0.375.) To make the interface kinetic contribution vanish at order Δx^2 we choose

$$f_k(\hat{n})=\frac{1-3\delta+4\delta(\partial_x^4\phi+\partial_z^4\phi)/|\vec{\nabla}\phi|^4}{1+\delta}, \tag{56}$$

TABLE I. List of the phase-field computational parameters used in dendritic growth simulations. These parameters yield an effective 3% anisotropy in surface energy and a diverging interface kinetic coefficient μ as defined here in Eq. (3).

Δx	0.8
Δt	0.06
D	2
Λ	3.268
$\overline{d}_0$	0.27
ϵ_4	0.03266
ϵ_e	0.03
δ	0.046

where the value of δ is computed, together with an order Δx^2 correction to Λ, in order to make $1/\mu$ vanish in Eq. (3), as described in [21]. The resulting computational parameters are summarized in Table I.

Lastly, in terms of our dimensionless units, where length, time, and velocity, are scaled in units of W, τ, and W/τ, respectively, and without interface kinetics, the thin-interface limit of the phase-field model is the standard free-boundary problem:

$$\partial_t u=D\,\nabla^2 u-\vec{\nabla}\cdot\vec{q}, \tag{57}$$

$$V_n=-D\,\hat{n}\cdot(\vec{\nabla}u|_l-\vec{\nabla}u|_s)+\hat{n}\cdot(\vec{q}|_l-\vec{q}|_s), \tag{58}$$

$$u_I=-\overline{d}_0(1-15\epsilon_e\cos 4\alpha)\,\kappa, \tag{59}$$

where $\vec{q}$ is the same noise as in the phase-field model and $\alpha=\cos^{-1}(\hat{z}\cdot\hat{n})$ is the angle of the normal measured from the z axis.

V. DENDRITIC SIDEBRANCHING

In this section, we simulate the phase-field model defined by Eqs. (42) and (53) to investigate sidebranching characteristics for different noise levels and a fixed dimensionless undercooling $\Delta\equiv(T_M-T_\infty)/(L/c)=0.55$, where T_∞ is the initial temperature of the melt. We then compare these results quantitatively with the predictions of the linear WKB theory that corresponds to the sharp-interface model defined by Eqs. (57)–(59).

A. Numerical results

Test simulations were first carried out with both noises, θ and $\vec{q}$, and with only the conserved noise $\vec{q}$. We found that time-averaged sidebranching characteristics were identical for the two cases within our numerical resolution. This finding shows that fluctuations which become amplified to produce sidebranches are on length scales much larger than the interface thickness, and thus driven solely by the bulk noise in agreement with expectation (see Sec. I and [27]). Consequently, all the results presented in this section were obtained with simulations where noise is added only to the heat transport equation (42). This represents a non-negligible computational saving for long simulation runs (i.e., two instead of three random numbers per site at each time step).

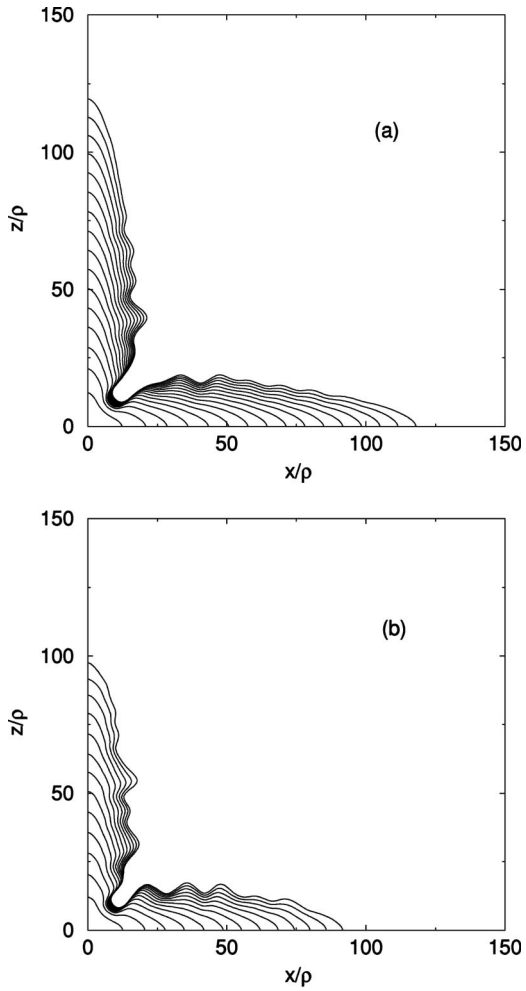

FIG. 2. Morphological development of a solid seed for $\Delta = 0.55$ and two different conserved noise amplitudes: (a) $F_u = 10^{-4}$, and (b) $F_u = 10^{-3}$. Other computational parameters are listed in Table I. The interfaces are plotted every 16 000 iterations.

The development of a dendrite and its sidebranches from a small initial seed is illustrated in Figs. 2(a) and 2(b) for two different noise levels. These simulations were carried out on a large 1200×1200 lattice with no-flux boundary conditions and, as initial condition, $u = 0$ and $\phi = 1$ inside a small circle in the lower left-hand corner of the quadrant and $u = -\Delta$ and $\phi = -1$ outside this circle. Note that in Fig. 2(b) the noise is sufficiently large to disturb the steady-state growth of the tip, which can be deduced from the fact that the vertical branch has outgrown the horizontal branch in this case. Since the tips do not interact via the diffusion field at this undercooling, i.e., the separation between the tips is much larger than the diffusion length, this difference can only be due to noise. This effect is negligible for the smaller noise level [Fig. 2(a)] where the two tips grew at nearly the same rate.

To investigate sidebranching, we restrict our attention to small noise levels ($F_u = 2.5 \times 10^{-5}$ and $F_u = 2.5 \times 10^{-4}$) with a well-defined steady-state tip structure. The symmetric growth of one tip about the z axis (i.e., half the dendrite with reflection symmetry) is simulated on lattices of size 300×400 and 300×600 with no-flux boundary conditions for, respectively, the larger and smaller noise amplitude (where sidebranches form further behind the tip). The same initial

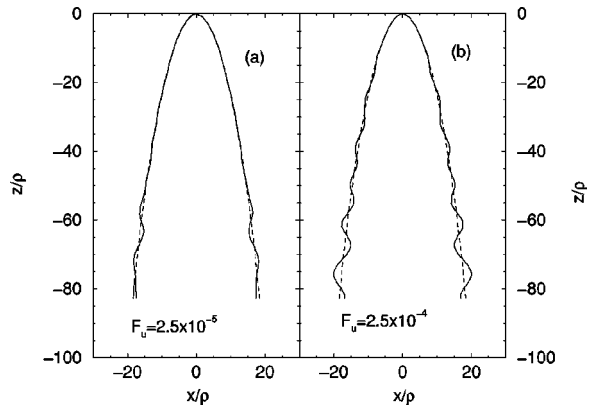

FIG. 3. Snapshots of the time-dependent dendrite shapes (solid lines) in long simulation runs that focus on the growth of one tip for $\Delta = 0.55$ and the parameters of Table I. The noiseless shape (dashed line) is superimposed for comparison. The noise levels are $F_u = 2.5 \times 10^{-5}$ in (a) and $F_u = 2.5 \times 10^{-4}$ in (b). Note that sidebranches form further behind the tip for the smaller noise level.

condition is used as in Fig. 2. As in Ref. [21], we periodically translate the entire structure in the opposite direction of growth to allow long simulation runs to be carried out in the smallest lattice size possible. Of course, we make sure that the sidebranching activity is not affected by this procedure by choosing a reasonable buffer larger than the diffusion length, and by carrying out test runs with larger lattice sizes. The constraint of symmetric growth prevents us from investigating the correlation of the sidebranching activity on opposite sides of the growth axis, which has been examined experimentally. However, it permits a more efficient investigation of the sidebranching amplitude and wavelength which can be compared to analytical predictions.

To calculate these two quantities, we proceed in two steps. First, we carry out a simulation without noise to obtain a ''reference'' steady-state (needle crystal) shape, without sidebranching. It is useful to measure this shape by the horizontal distance $x_0(z)$ of the interface measured from the vertical growth axis as a function of the distance z behind the tip. This distance is calculated by numerical interpolation of the $\phi = 0$ contour. The steady-state operating state of the dendrite is defined in terms of the dimensionless tip velocity and radius

$$\tilde{V} = V\overline{d_0}/D, \tag{60}$$

$$\tilde{\rho} = \rho/\overline{d_0}. \tag{61}$$

For the present choice of undercooling and anisotropy, we find that $\tilde{V} = Vd_0/D \approx 0.011$ and $\tilde{\rho} = \rho/d_0 \approx 21.8$. These results are in excellent quantitative agreement with the exact benchmark predictions of solvability theory (valid for an arbitrary anisotropy) obtained by solving numerically the two-dimensional (2D) steady-state growth sharp-interface equations by boundary integral method [21,35–38]. Second, we add the conserved noise to the heat equation and calculate the time-dependent shape, $x(z,t)$, with sidebranching present. Snapshots of noisy shapes superimposed on the noiseless shape are illustrated in Fig. 3. Examples of time traces of $x(z,t)$ for two different distances behind the tip are

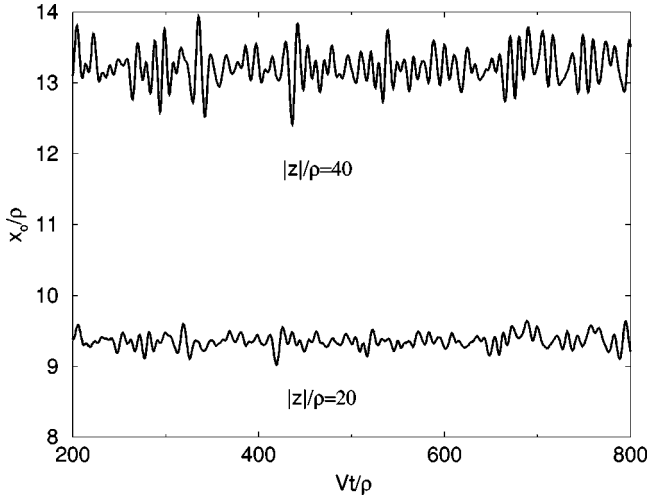

FIG. 4. Horizontal position of the interface measured from the vertical growth axis as a function of dimensionless time at 20 and at 40 tip radii behind the tip. The parameters are the same as in Fig. 3(a).

shown in Fig. 4. In addition, an example of the noise-averaged power spectrum of a long time trace is shown in Fig. 5. This spectrum was calculated by subdividing the complete time interval into several equal subintervals, then calculating the power spectrum for each subinterval, and finally taking the average of these power spectra.

In terms of the above quantities, the root-mean-square amplitude of sidebranches is simply given by

$$A(z)=\sqrt{\langle[x(z,t)-x_0(z)]^2\rangle}, \tag{62}$$

where the average is over time. This quantity is plotted vs z in Fig. 6 for two different noise levels. To obtain good statistics, we typically simulated a total time of $2000V/\rho$ which took 200–350 CPU hours on a high end workstation. The mean spacing between sidebranches (sidebranching wavelength) $\langle\lambda(z)\rangle$ can be calculated in two ways. One way, which corresponds more directly to the way in which this quantity is calculated in the WKB theory discussed below, is to define

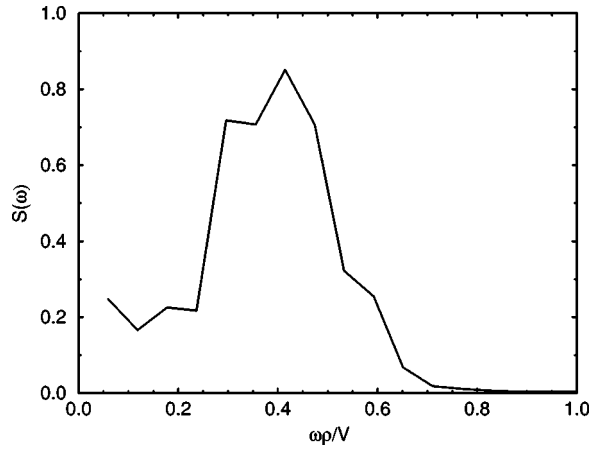

FIG. 5. Noise-averaged power spectrum of $x(z,t)$ at $|z|/\rho=40$ for $F_u=2.5\times10^{-5}$.

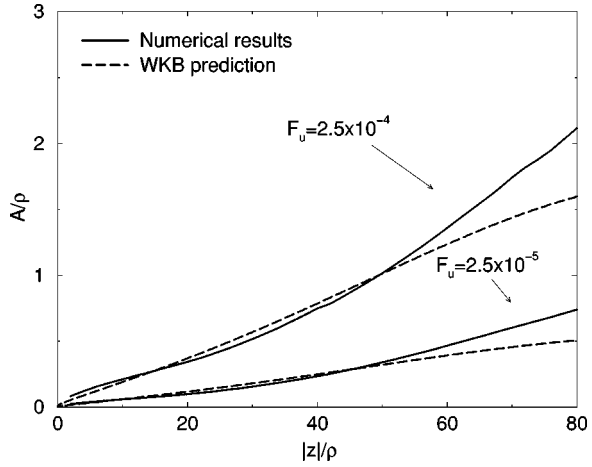

FIG. 6. Root-mean-square amplitude of sidebranches as a function of distance behind the tip for two different noise levels in the simulations (solid lines). Superimposed are dashed lines corresponding to the analytical predictions of Eq. (65).

$$\langle\lambda(z)\rangle=\frac{2\pi V}{\omega_c(z)}, \tag{63}$$

where ω_c is the peak frequency of the power spectrum of $x(z,t)$, averaged over sufficiently long time. An alternate, and faster way, which avoids calculating the power spectrum, is to count the number $N(z)$ of extrema of $x(z,t)$ in a long time interval $t_1\leqslant t\leqslant t_2$. Simple node counting then leads to the relation

$$\langle\lambda(z)\rangle=\frac{2V(t_2-t_1)}{N(z)}. \tag{64}$$

For the spectrum of Fig. 5, these two methods yield similar values: $\langle\lambda(z)\rangle/\rho\approx15$ as calculated from Eq. (63) with $\omega_c\approx0.42$ extracted from Fig. 5 and $\lambda(z)/\rho=13.5$ as calculated numerically from Eq. (64). Consequently, we have used Eq. (64) to calculate $\langle\lambda(z)\rangle$ vs z and the result for the lowest noise level is shown in Fig. 7.

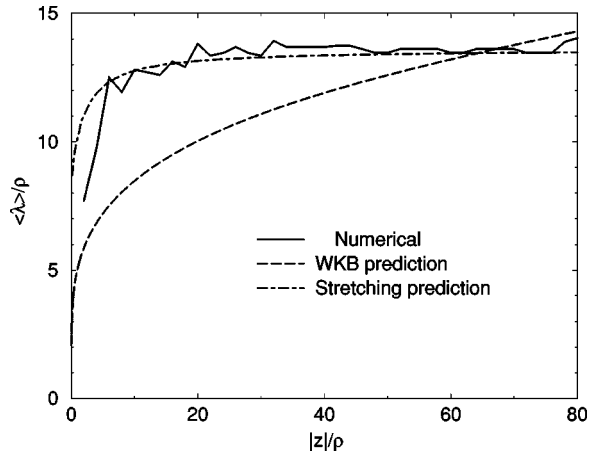

FIG. 7. Mean spacing of sidebranches as a function of distance behind the tip in the simulation for $F_u=2.5\times10^{-5}$ (solid line), analytically predicted by Eq. (66) (dashed line) and predicted on the basis of stretching (dash-dotted line).

B. Comparison with linear WKB theory

Langer [10] and Brener and Temkin [11] have analyzed noise-induced sidebranching in three dimensions for specific needle crystal shapes (i.e., $x \sim z^{1/2}$ and $x \sim z^{3/5}$). It is straightforward to extend their analyses, based on a WKB approach, to an arbitrary needle crystal shape, $x_0(z)$, in d dimension [39]. We shall only state here the final results necessary to interpret our simulations. The expressions for the sidebranching amplitude and wavelength are given, respectively, by [39]

$$\overline{A}(\overline{z}) = \overline{S} \exp\left(\frac{2}{3} \left[\frac{\overline{x_0^3}}{3\,\sigma^* \overline{z}} \right]^{1/2} \right), \tag{65}$$

$$\langle \overline{\lambda}(\overline{z}) \rangle = \frac{2\pi}{\overline{\omega_c}} = \pi \left[\frac{12 \sigma^* \overline{z}}{\overline{x_0}} \right]^{1/2}, \tag{66}$$

where we have defined the scaled quantities $\overline{x_0} = x_0/\rho$, $\overline{z} = -z/\rho$, $\overline{A} = A/\rho$, $\overline{\lambda} = \lambda/\rho$, $\overline{\omega_c} = \omega_c \rho / V$, the dimensionless noise amplitude $\overline{S}$, given by

$$\overline{S^2} = \frac{2F_u D}{\rho^{1+d} V} = \frac{2F_u}{\overline{d_0^d}\, \tilde{\rho}^{1+d} \tilde{V}} \qquad (d = 2,3), \tag{67}$$

and

$$\sigma^* \equiv \frac{2D\overline{d_0}}{\rho^2 V} = \frac{2}{\tilde{\rho}^2 \tilde{V}}. \tag{68}$$

It is easy to check that Eqs. (65) and (66) reduce to the earlier results of Refs. [10,11] if specific shapes (parabola and 3/5 law) are substituted into them. Note that if we convert back to dimensional units by letting $\rho \to \rho/W$, $V \to V\tau/W$, and $D \to D\tau/W^2$, in Eq. (67), we obtain the expression

$$\overline{S^2} = \frac{2 k_B T_M^2\, c\, D}{L^2 \rho^{1+d} V}, \tag{69}$$

which is dimensionless if one interprets L and cT_M to have dimension of energy/(length)^d. Of course, this interpretation is only physically meaningful in three dimensions where Eq. (69) becomes identical to the definition of $\overline{S}$ in Ref. [10]. Therefore, in the present study we evaluate $\overline{S}$ directly from Eq. (67) to compare simulations and theory. For $\overline{d_0} = 0.27$ (Table I) and the aforementioned selected values, $\tilde{V} \approx 0.011$ and $\tilde{\rho} \approx 21.8$, we obtain $\overline{S} \approx 0.24 F_u$ and $\sigma^* \approx 0.383$. (Note that σ^* is larger here than in experiment due to both the large value of anisotropy which produces a pointy tip, and the fact that σ^* is larger in 2D than 3D for the same anisotropy.) The analytical predictions for the sidebranching amplitude and wavelength are then simply obtained by putting these values into Eqs. (65) and (66) together with the steady-state interface shape, $\overline{x_0}(\overline{z})$, measured in the noiseless phase-field simulation (dashed lines in Fig. 3).

Figures 6 and 7 show that the amplitude and wavelength measured in the phase-field simulations with noise are in good overall quantitative agreement with the analytical predictions even though σ^* is not much smaller than one. The amplitude in the simulations is relatively well predicted by Eq. (65), up to a certain distance behind the tip after which the two curves depart from each other. This departure may be due to nonlinear effects which become important when $\overline{A}$ becomes of order unity. In addition, it should be emphasized that the prefactor of Eq. (65) is only known up to some multiplicative factor of order unity. Consequently, what is more relevant here is that the amplitudes in simulation and theory are of comparable magnitude, rather than the fact that the numerical and theoretical curves in Fig. 6 seem to almost perfectly overlap up to $\overline{z} \simeq 20$, which may be coincidental.

The wavelength in the simulations is only about 30% larger than predicted by Eq. (66) in the region (20 to 40 tip radii behind the tip) where sidebranches become visible. However, this wavelength increases initially faster with distance behind the tip than predicted. One possible explanation for this faster rate of increase is that perturbations generally get stretched as they travel along the sides of curved fronts [4–6]. To test this possibility, let us calculate the purely deterministic change of wavelength of a perturbation initially at the tip due to stretching. The rate of stretching is given by [4–6]

$$\frac{1}{\lambda} \frac{d\lambda}{dt} = \frac{\partial V_t}{\partial s}, \tag{70}$$

where $V_t = V \sin\alpha$ is the tangential velocity of advection of the perturbation and s measures the arc length along the interface. Equation (70) is strictly valid in the WKB limit where λ is small compared to the local radius of curvature $(1/\kappa)$ of the interface. We can solve Eq. (70) by using the change of variable $dt = dz/V$. Equation (70) becomes then $d(\ln\lambda) = \sin 2\alpha d\alpha/2$, which can be easily integrated. Furthermore, using the geometrical relation, $\cos\alpha = 1/[1 + (d\overline{x_0}/d\overline{z})^2]^{1/2}$, we obtain

$$\overline{\lambda}(\overline{z}) = \overline{\lambda}_\infty \exp\left[-\frac{1}{2} \frac{(d\overline{x_0}/d\overline{z})^2}{1 + (d\overline{x_0}/d\overline{z})^2} \right], \tag{71}$$

where we have defined $\overline{\lambda}_\infty$ to be the saturation value of $\overline{\lambda}$ far behind the tip (i.e., $\overline{z} \to \infty$). It should be emphasized that the value of $\overline{\lambda}_\infty$ cannot be predicted alone by Eq. (71) since this equation does not describe the selective amplification of noise at the tip. The prediction of $\langle \overline{\lambda} \rangle$ at a given distance from the tip still requires the WKB analysis. Equation (71), however, can be used to estimate the relative change of wavelength due to stretching. Thus it is reasonable to use the value of $\overline{\lambda}_\infty$ observed in simulation (i.e., the saturation value of the solid line at large $|z|$ in Fig. 7) as input into Eq. (71) in order to test whether the faster increase in spacing in the tip region observed in simulation, as compared to the WKB prediction, may be due to stretching. For this purpose, we have plotted in Fig. 7 the prediction of Eq. (71) with the value of $\overline{\lambda}_\infty \approx 13.5$ that corresponds to the large $|z|$ plateau of the solid line. We can see that this prediction gives indeed a better agreement with simulation near the tip for the mean spacing, which indicates that stretching is likely to be the

origin of the disagreement between simulation and the WKB theory in this region. Indeed, this stretching effect has been neglected in the WKB calculations to date that are only strictly valid in the far tip region ($\bar{z} \gg 1$), where this effect is negligibly small. It should, however, be possible in the future to carry out a more elaborate noise amplification calculation that incorporates this effect and that should in principle yield an improved prediction of the sidebranch spacing near the tip.

Finally, we note that the sidebranching wavelength is about an order of magnitude larger than the tip radius in our simulations, whereas it is only a factor of 2 or 3 in the experiments of Huang and Glicksman in succinonitrile [3]. This difference is due to the fact that σ^* is much larger here than in these experiments because of the larger value of anisotropy used in simulations.

VI. CONCLUSIONS

We have presented a phase-field model of the solidification of a pure melt that incorporates thermal noise quantitatively. From a computational standpoint, there are two main conclusions regarding the incorporation of this noise. First, one can retain the freedom to choose the interface thickness at will as long as the noise magnitude (F_u) that enters in the phase-field model is scaled appropriately [Eq. (46)]. Therefore, it remains possible to carry out dramatically more efficient computations without interface kinetics by choosing $\bar{d}_0$ substantially smaller than unity, as in our earlier studies without noise [21]. Secondly, for typical growth conditions at low undercooling (and, more generally, below a critical velocity that depends on the attachment kinetic coefficient μ), the conserved noise in the heat current is the most relevant one. This noise drives long-wavelength interface fluctuations that become amplified to a macroscopic scale by the morphological instability on the sides of dendrites. In contrast, the nonconserved noise in the evolution equation for ϕ drives short-wavelength fluctuations that are damped and do not affect sidebranching, as predicted by a sharp-interface analysis [27] and confirmed by our simulations. Consequently, this noise can be left out in computations below this critical velocity.

We have applied this model to carry out a detailed quantitative study of the initial stage of sidebranch formation during dendritic growth. We conclude that the root-mean-square sidebranching amplitude is reasonably well predicted by the existing linear WKB theory of noise amplification, even though the value of σ^* in our simulations is not small. In addition, the WKB theory gives a reasonable estimate of the spacing between sidebranches at the distance behind the tip where they become of amplitude comparable to the tip radius. It does not, however, accurately predict the functional form of the variation of this spacing with distance behind the tip for the present phase-field simulations. This leaves open the question as to why the sidebranch amplitude is better predicted in the tip region than the sidebranch spacing by the existing WKB theory, at least for the present simulations. In the simulations, this spacing increases faster behind the tip than predicted by this theory. We have argued on the basis of a simple analytical estimate that this faster rate of increase may be due to stretching but a more elaborate noise amplification calculation that incorporates this effect is needed to validate this conjecture. Nonetheless, the overall quantitative agreement between theory and simulation can be viewed to be reasonably satisfactory given the lack of any adjustable parameters and the intrinsic limitations of the WKB approximation.

A more stringent test of this theory would require us to extend the present study to a range of smaller anisotropy, and hence smaller σ^*, where a comparison between this theory and simulations is more justified. Another interesting problem that was not investigated here is the evolution of the sidebranch spacing even further away from the tip due to the growth competition between sidebranches [11,40]. Finally, since this study has been restricted to two dimensions, we cannot yet answer the important question of whether thermal noise alone is responsible for the sidebranching activity observed in experiment. Simulations in three dimensions should provide a clearcut answer to this question.

ACKNOWLEDGMENTS

We thank Mathis Plapp for valuable suggestions concerning the numerical treatment of the conserved noise. This work was supported by DOE Grant No. DE-FG02-92ER45471 and benefited from Cray T3E time at the National Energy Resources Supercomputer Center (NERSC) and time allocation at the Northeastern University Advanced Scientific Computation Center (NU-ASCC).

[1] W. Kurz and D. J. Fisher, *Fundamentals of Solidification* (Trans Tech, Aedermannsdorf, Switzerland, 1989).
[2] R. Trivedi and W. Kurz, Int. Mater. Rev. **39**, 49 (1994).
[3] C. Huang and M. E. Glicksman, Acta Metall. **29**, 701 (1981); **29**, 717 (1981).
[4] P. Pelce, Ph.D. thesis, Université de Provence, 1986.
[5] P. Pecle and P. Clavin, Europhys. Lett. **3**, 907 (1987).
[6] Ya. B. Zel'dovich, A. G. Istratov, N. I. Kidin, and V. B. Librovich, Combust. Sci. Technol. **24**, 1 (1980).
[7] R. Pieters and J. S. Langer, Phys. Rev. Lett. **56**, 1948 (1986).
[8] M. Barber, A. Barbieri, and J. S. Langer, Phys. Rev. A **36**, 3340 (1987).
[9] D. Kessler and H. Levine, Europhys. Lett. **4**, 215 (1987).
[10] J. S. Langer, Phys. Rev. A **36**, 3350 (1987).
[11] E. Brener and D. Temkin, Phys. Rev. E **51**, 351 (1995).
[12] A. Dougherty, P. D. Kaplan, and J. P. Gollub, Phys. Rev. Lett. **58**, 1652 (1987).
[13] U. Bisang and J. H. Bilgram, Phys. Rev. Lett. **75**, 3898 (1995).
[14] R. Almgren, W. S. Dai, and V. Hakim, Phys. Rev. Lett. **71**, 3461 (1993).
[15] E. Brener, Phys. Rev. Lett. **71**, 3653 (1993).
[16] J. C. LaCombe, M. B. Koss, V. E. Fradkov, and M. E. Glicksman, Phys. Rev. E **52**, 2778 (1995).
[17] A. A. Wheeler, B. T. Murray, and R. Schaefer, Physica D **66**, 243 (1993).
[18] J. A. Warren and W. J. Boettinger, Acta Metall. Mater. **43**, 689 (1995).

[19] S-L. Wang and R. F. Sekerka, Phys. Rev. E **53**, 3760 (1996).
[20] B. T. Murray, A. A. Wheeler, and M. E. Glicksman, J. Cryst. Growth **47**, 386 (1995).
[21] A. Karma and W. J. Rappel, Phys. Rev. E **53**, R3017 (1996); Phys. Rev. Lett. **77**, 4050 (1996); Phys. Rev. E **57**, 4323 (1998).
[22] N. Provatas, N. Goldenfeld, and J. Dantzig, Phys. Rev. Lett. **80**, 3308 (1998); J. Comp. Phys. (to be published).
[23] T. Ihle and H. Muller-Krumbhaar, Phys. Rev. E **49**, 2972 (1994).
[24] J. S. Langer, *Directions in Condensed Matter*, edited by G. Grinstein and G. Mazenko (World Scientific, Singapore, 1986), p. 164.
[25] J. B. Collins and H. Levine, Phys. Rev. B **31**, 6119 (1985).
[26] B. I. Halperin, P. C. Hohenberg, and S-K. Ma, Phys. Rev. B **10**, 139 (1974).
[27] A. Karma, Phys. Rev. Lett. **70**, 3439 (1993); Phys. Rev. E **48**, 3441 (1993).
[28] L. D. Landau and E. M. Lifshitz, *Statistical Physics* (Pergamon, New York, 1980).
[29] G. Caginalp and X. Chen, in *On the Evolution of Phase Boundaries*, edited by M. E. Gurtin and G. B. McFadden, The IMA Volumes in Mathematics and Its Applications Vol. 43 (Springer-Verlag, New York, 1992), p. 1.
[30] The coupling constant is denoted by Λ, in place of λ in Ref. [21], since λ is used here to denote the wavelength of fluctuations or the spacing between sidebranches.
[31] R. Kobayashi, Physica D **63**, 410 (1993); Experimental Math. **3**, 60 (1994).
[32] S-L. Wang, R. F. Sekerka, A. A. Wheeler, B. T. Murray, S. R. Coriell, R. J. Braun, and G. B. McFadden, Physica D **69**, 189 (1993).
[33] M. E. Glicksman and N. B. Singh, J. Cryst. Growth **98**, 277 (1989).
[34] M. Muschol, D. Liu, and H. Z. Cummins, Phys. Rev. A **46**, 1038 (1992).
[35] J. S. Langer, in *Chance and Matter*, Lectures on the Theory of Pattern Formation, Les Houches, Session XLVI, edited by J. Souletie, J. Vannimenus, and R. Stora (North-Holland, Amsterdam, 1987), pp. 629–711; D. Kessler, J. Koplik, and H. Levine, Adv. Phys. **37**, 255 (1988); E. A. Brener and V. I. Melnikaov, *ibid.* **40**, 50 (1991).
[36] D. A. Kessler and H. Levine, Phys. Rev. B **33**, 7867 (1986).
[37] D. I. Meiron, Phys. Rev. A **33**, 2704 (1986).
[38] M. Ben Amar and B. Moussallam, Physica D **25**, 155 (1987).
[39] A. Karma (unpublished).
[40] Q. Li and C. Beckermann, Phys. Rev. E **57**, 3176 (1998).